Physics of Plasmas

RESEARCH ARTICLE | AUGUST 03 2023

Experimental observation of a field-aligned ion beam produced by magnetic reconnection of two flux ropes FREE

S. W. Tang ; W. Gekelman ; R. D. Sydora

Phys. Plasmas 30, 082104 (2023)
https://doi.org/10.1063/5.0138350
CHORUS

Experimental observation of a field-aligned ion beam produced by magnetic reconnection of two flux ropes

Cite as: Phys. Plasmas **30**, 082104 (2023); doi: 10.1063/5.0138350
Submitted: 11 December 2022 · Accepted: 11 July 2023 ·
Published Online: 3 August 2023

S. W. Tang,[1,2,a] W. Gekelman,[1] and R. D. Sydora[3]

AFFILIATIONS

[1]Basic Plasma Science Facility, University of California Los Angeles, 1000 Veteran Avenue, Room 15-70, Los Angeles, California 90095-1696, USA
[2]University of California San Diego, 9500 Gilman Drive, La Jolla, California 92093, USA
[3]University of Alberta, 116 Street & 85 Avenue, Edmonton, Alberta T6G 2R3, Canada

[a]Author to whom correspondence should be addressed: swjtang@ucsd.edu

ABSTRACT

An ion beam field-aligned to the background guide field ($B_0 = 330$ G) was observed in a reconnection experiment on the Large Plasma Device and, to the authors' knowledge, is the first experimental observation of its kind. Two kink-unstable flux ropes ($L = 11$ m, $d = 7.6$ cm) were made to collide, which allows magnetic reconnection to occur. Sub-Alfvénic ion beams with energies of up to 15 eV were then observed from measurements of the local ion energy distribution function. The beam ions do not appear to be heated. They were correlated with the collision of the ropes and appear to be energized by magnetic reconnection. The results and interpretation of the measurements are supported by three-dimensional gyrokinetic particle simulations of the merging flux ropes and electric field measurements from previous experiments [W. Gekelman *et al.*, Astrophys. J. **853**, 33 (2018)]. The mechanism behind the acceleration appears to be non-local.

I. BACKGROUND

Magnetic reconnection is a process in which the topology of the magnetic field changes, resulting in the conversion of magnetic energy to heat or electric fields that can respectively energize or accelerate particles.[1–3] A large variety of plasma waves with varying frequency ranges can also be generated, thereby creating turbulent and non-linear effects that influence the large-scale dynamics of the surrounding region.[4,5]

In laboratory studies of ion energization associated with magnetic reconnection, two spherical or toroidal magnetized plasmas are often merged to induce reconnection. Examples include the TS-3 device, where ions were heated up to 200 eV and were accelerated to Alfvénic velocities;[6] the Magnetic Reconnection Experiment (MRX), where sub-Alfvénic ion flows, not beams, both parallel and perpendicular to the local magnetic field were observed with localized ion heating;[7] and the Swarthmore Spheromak Experiment (SSX), where 70 eV protons moving within the plane of reconnection[8] and super-Alfvénic ions with energies in excess of 100 eV were observed in the direction normal to the reconnection plane.[9] The super-Alfvénic ions in the SSX were consistent with test particle simulations and were correlated with 3D reconnection events.

While most experiments involving reconnection can be adequately described by two-dimensional models, the geometry of reconnection is inherently three-dimensional.[10] Therefore, systems that are described by three-dimensional reconnection models such as magnetic flux ropes are very appropriate for studying ion energization. Flux ropes are current-carrying columns of plasma that are abundant in space and play a major role in the study of astrophysical plasmas, such as those found in the solar photosphere and corona.[11,12] They can become kink-unstable by carrying a sufficiently large current, which then causes the ropes to writhe, twist, and collide with each other, thereby triggering magnetic reconnection.[13] As a result, evidence of ion heating and acceleration could be observed during the reconnection events of solar flares and coronal mass ejections,[2,14] as well as from ion flows within the Earth's magnetotail,[15] where the behavior of ions was studied using kinetic simulations.[16,17]

In this study, the energization of ions due to the collision of two flux ropes in the Large Plasma Device (LAPD) is explored.[18] The morphology of the LAPD flux ropes and the various reconnection regions were well quantified through topological studies[19,20] that identified the quasi-sepratrix layer (QSL), which measures the three-dimensional separation of field lines.[21–24] The topological winding number, a

mathematical quantity that measures the entanglement of field line pairs, subsequently identified regions of reconnection that were not observed in the QSL.[25] In this experiment, once the reconnection regions of the ropes were identified, the local ion energy distribution function (IEDF) was measured with a retarding field energy analyzer (RFEA), and evidence of ion energization related to the reconnection of two flux ropes was observed. The results were then compared to three-dimensional gyrokinetic particle simulations (see Sec. VII), which showed agreement with the experimental findings.

II. EXPERIMENTAL SETUP

Figure 1 shows the experimental setup of the two flux ropes on the LAPD. The vacuum chamber is 26.5 m long and backfilled with helium (base pressure 2.7×10^{-5} Torr). The background plasma ($n_e = 1 \times 10^{12}$ cm^{-3}, $T_e \sim 4$ eV, $T_i \sim 1$ eV) is a 60 cm wide cylindrical column produced by a lanthanium hexaboride (LaB_6) cathode and molybdenum anode pair located at one end of the chamber. A second LaB_6 cathode produces a denser current carrying plasma ($n_e = 2 \times 10^{12}$ cm^{-3}, $T_e \sim 7$ eV, $T_i \sim 4$ eV) from the other end of the chamber. The current flows through an electrically floating carbon mask that has two 7.6 cm diameter holes with an edge-to-edge separation of 3 cm. A stainless steel anode located $\Delta z = 11$ m away from the carbon mask terminates the rope currents, and the length of the ropes is defined by the cathode–anode separation. The experiment is conducted in a $B_0 = 330$ G background field strong enough to magnetize the ions and electrons throughout ($\beta < 0.01$).

For the sake of brevity, the details of the design, construction, and operational considerations of the ion RFEA used in this experiment will be presented in a standalone paper to be published elsewhere.[26] A brief description of the RFEA is thus as follows. The RFEA probe head consists of four circular stainless steel grid meshes and a tantalum disk-shaped collector. These components are electrically isolated from each other using 50–100 μm thick mica washers. Each grid mesh has an opening size of 43.2 μm and a transparency of 30%, except for the entrance grid. The entrance grid is comprised of four grids stacked together, which attenuates the density of the incoming plasma to less than 1%. The separation between the grids is 1.3 mm, and the effective area of the probe is 71 mm^2 (with diameter 9.52 mm). The grids and collector are housed in a cylindrical shell made of nonporous alumina ceramic. The probe head has a length of 15 mm and an outer diameter of 15.9 mm.

The repeller grid (grid #1) was biased at −50 V to repel electrons entering the RFEA. During the experiment, it was discovered that connecting the entrance grid (grid #0) to the repeller grid resulted in a less noisy collector current and significantly improved measurements. As a result, the RFEA effectively operated as a three-grid energy analyzer, with the entrance grid biased at −50 V. To repel secondary electrons emitted from the collector, the suppressor grid (grid #3) was biased at −9 V relative to the collector, which was itself biased at −67.5 V to repel electrons and collect ions. Therefore, the potential of the suppressor grid was −76.5 V.

To determine the IEDF of the plasma, the collector current I was measured as a function of the discriminator grid (grid #2) voltage V to obtain an I–V characteristic at a fixed location in the plasma. The collector current I depends on the IEDF or $f(E)$ as

$$I = \frac{ZeA}{m} \int_{e(V-V_p)}^{\infty} dE f(E), \tag{1}$$

where Z and m are the effective nuclear charge and mass of the ion, respectively (in our case, $Z = 1$), e is the elementary charge, A is the effective area of the probe, and V_p is the plasma potential. By differentiating Eq. (1) with respect to V, a function proportional to the IEDF is then obtained.

It may be noted that unlike most energy analyzers, the voltage on the discriminator grid V cannot be rapidly increased within a short time interval to obtain an I–V curve due to an unusually high internal capacitance of the RFEA. The latter produces an unwanted capacitive current that is typically larger than the collector current of the RFEA. Therefore, to avoid this situation, V was increased in steps. It was first fixed at a given potential for the duration of a single data shot and then incremented by a small amount on the next data shot. In this manner, the voltage was increased from 0 to 110 V in step sizes of 0.25 V, while the RFEA was at a single location. Each step consisted of 100 shots that were conditionally averaged to smooth out the noise and correct for the random phase of each shot that would cause the coherent mode oscillation of the flux ropes to start at different times. This involves shifting each shot in time corresponding to a phase relative to a chosen shot from a B-dot probe[27] that was fixed in position near the RFEA before taking the average.[28] The conditionally averaged data points from the 441 different voltage steps were then combined to construct an I–V curve. Overall, this process is more time-intensive when compared to a regular voltage sweep as more data have to be collected to construct the I–V curve at a single location for a given set of parameters, which can take up to a full day of machine time. However, a benefit of this method is that I–V curves can be constructed for any time during the experiment when the flux ropes are present. The time uncertainty of each IEDF is thus the sampling rate of the data acquisition system, which is 0.32 μs (= 1/3.125 MHz).

In this experiment, data were acquired with flux ropes from two different cases that were conducted in two separate experimental

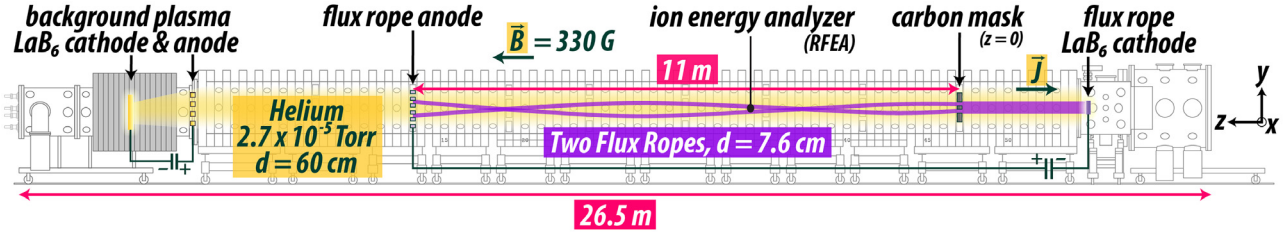

FIG. 1. A scale drawing of the experimental setup and the various components used to create the two flux ropes on the LAPD. The location of the RFEA (ion energy analyzer) is shown, while the coordinate system is displayed on the far right.

sessions. In case 1, only RFEA data were collected. Magnetic field and vector potential measurements were not available. Measurements were made with the RFEA facing both directions along $(\pm z)$ and across $(\pm y)$ the magnetic field when it was located at $(x, y, z) = (3.4, 0.0, 420)$ cm, but only in the $+z$ direction at $(x, y, z) = (10, 0.0, 420)$ cm. The discharge potential of the flux rope cathode was $V_D = 120$ V, while the current that flowed through each rope was $I_R = 610$ A. In contrast, case 2 contains planar B-dot probe measurements that were made in conjunction with the RFEA. The RFEA data, however, were limited to ions moving only in the z-direction. In this case, the RFEA was located at $(x, y, z) = (6.0, 1.7, 540)$ cm. The discharge potential was $V_D = 140$ V, and the current through a single rope was $I_R = 550$ A. In both cases, the ropes were initially centered at $(x, y) = (0, 0)$ cm. In the sections that follow, data from case 1 are presented in Secs. III–V, while data from case 2 are presented in Sec. VI.

III. BI-MAXWELLIAN DERIVATIVES OF THE *I–V* CHARACTERISTIC

Figure 2(a) shows an I–V curve constructed from the conditionally averaged data points and then digitally smoothed using a Savitzky–Golay filter. The I–V curve is characterized by a flat region of ion saturation current when the discriminator grid voltage V is below the local plasma potential V_p. The current then decays to zero as V is increased. In this example, the value of V that corresponds to zero ion energy (i.e., the transition point where the ion current no longer saturates and starts to decay) is approximately near 60 V in part due to the -50 V applied on the entrance grid.

The smoothed I–V curve is then differentiated to obtain a $-dI/dV$ curve, which is the blue line in Fig. 2(b). In each of the $-dI/dV$ curves produced, the large peaks tend to fit either a single Maxwellian or a bi-Maxwellian function which has the form

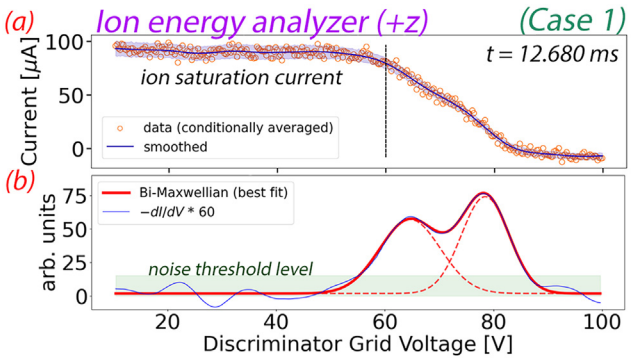

FIG. 2. (a) An I–V curve of the collector current I as a function of the discriminator grid voltage V is presented. The RFEA measures ions moving in the $+z$ direction. The orange data points represent the conditional average of 100 individual shots measured at the same V. The blue line represents the smoothed data, while the light blue region corresponds to its standard error. (b) A plot of $-dI/dV$ which represents the derivative of the I–V curve is shown. The smoothed raw data are depicted by the blue line. The best-fitting function (a bi-Maxwellian) is shown in red, along with the component Maxwellians indicated by the red dashed lines. The green region indicates the threshold level below which peaks are considered noise and are excluded in the fitting the $-dI/dV$ curve.

$$A_1 \exp\left(-\frac{(V - V_1)^2}{2b_1^2}\right) + A_2 \exp\left(-\frac{(V - V_2)^2}{2b_2^2}\right) + c, \quad (2)$$

where A_i, b_i, and V_i (for $i = 1$ and 2) are the fitting parameters that determine the height, width, and peak potential of the component Maxwellians, respectively, and c is the overall vertical offset of the plot. For a single Maxwellian, $A_2 = 0$. Then, the best-fitting function is determined by the function that gives the smallest least squares error. In the case of the $-dI/dV$ shown in Fig. 2(b), the best-fitting function is a bi-Maxwellian that is plotted in red. The component Maxwellians are indicated by the red dotted lines.

It may be noted that noisy oscillations were produced by numerical differentiation of the data and the use of a Savitzky–Golay filter during smoothing. These oscillations are visible at the regions where $-dI/dV$ is expected to be constant such as when the ion current saturates (i.e., $V < V_p$) or when the current is close to zero. The maximum height of these oscillations represents an error in the fit as the peaks in $-dI/dV$ were only fitted to a (bi-)Maxwellian if their amplitudes were greater than this level. This "noise threshold level," which is shown in Fig. 2(b), is different for every $-dI/dV$ plot and is recalculated for every instant in time a $-dI/dV$ plot is generated.

A $-dI/dV$ curve that best fits a bi-Maxwellian function suggests that an ion beam is present, which is represented by a more energetic secondary peak. Evidence of this is also provided by observing the time evolution of a single oscillation cycle of the flux ropes ($f = 3.9$ kHz) which contains a bi-Maxwellian $-dI/dV$ such as the one shown in Fig. 2(b). This is presented in Fig. 3, where eight evenly timed plots within a 0.256 ms interval are shown. The $-dI/dV$ curve initially fits a single Maxwellian, which is assumed to be the primary distribution of ions in the plasma. As the flux ropes oscillate, a secondary peak with an energy range of 9–15 eV develops and is most prominent at $\Delta t = +0.096$ ms. At this time, most ions from the primary distribution have been redistributed into the secondary peak. The best-fit function is also bimodal, which indicates that the function is comprised of a mixture of two distinct normal distribution of ions.[29] As the presence of the secondary peak persists longer than the reconnection timescale ($\tau = 50$ μs), it suggests that the ion beam is real.

As an aside, the beam energy is always measured with respect to the peak potential of the primary distribution, which changes with time due to the oscillation of the flux ropes. Figure 4 shows the peak potential of both the primary distribution and the beam plotted as a function of time when the flux ropes are present. The blue data points between 11 and 14 ms show that the peak potential of the primary distribution oscillates with a range of approximately 8–12 V, which is the same order of magnitude as the change in the plasma potential at a fixed point observed by an emissive probe in an previous experiment.[30] The orange data points are plotted for the peak potentials of the secondary distribution when $-dI/dV$ is a bi-Maxwellian. These points indicate when a beam is present and appears to be in phase with the oscillation of the primary distribution.

IV. THE ION ENERGY DISTRIBUTION FUNCTION AND DIRECTION OF ION BEAM PROPAGATION

A limitation of the RFEA is that it only measures ions moving in a single direction perpendicular to the face of the planar electrodes. Therefore, obtaining the IEDF along a single axis requires splicing two $-dI/dV$ measurements, where the second measurement has the

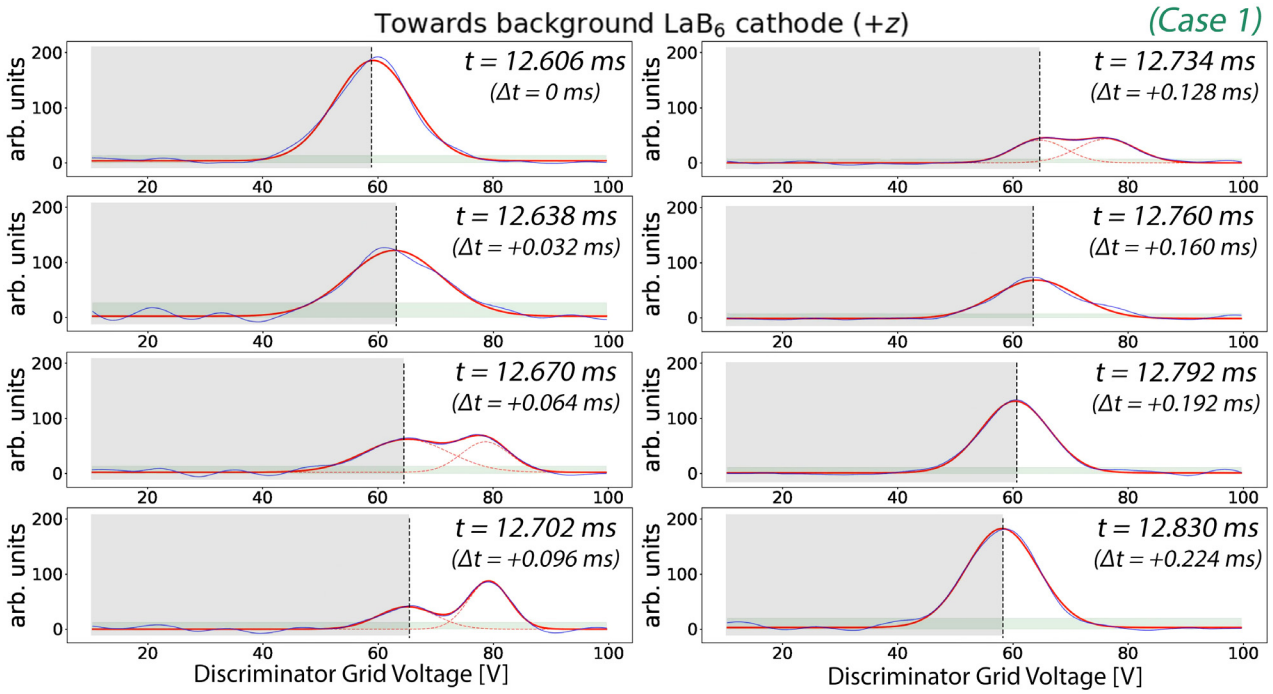

FIG. 3. The time evolution of $-dI/dV$ is shown, which illustrates the development of a beam for ions moving along the magnetic field in the $+z$ direction and away from the source of the ropes. The curves are plotted for the duration of a single flux rope oscillation ($\Delta t = 0.256$ ms). The dashed line estimates the plasma potential V_p and separates the gray region of ion saturation current from the rest of the $-dI/dV$ curve. A beam is clearly observed from the bi-Maxwellian function at $t = 12.702$ ms.

RFEA facing the direction directly opposite to the first. Figure 5 shows two examples of IEDFs constructed using this method. Figure 5(a) is comprised of two single-peaked distributions, while Fig. 5(b) is comprised of a single-peaked distribution and a bi-Maxwellian function.

In both these figures, the IEDF is plotted as a function of its energy E in which positive values of E represent ions moving in one direction and negative values represent ions moving in the opposite direction. Since the ions' energy are not discriminated when $V < V_p$, only the part of the $-dI/dV$ curve where $V \geq V_p$ is plotted. A change of variables is then applied where $-dI/dV$ is plotted as a function of E, where $E = e(V - V_p)$. The two curves are then joined at $E = 0$ which represents $V = V_p$ for both curves. In each of the $-dI/dV$ curves, the value of V_p is estimated to be the peak potential of a single Maxwellian or the peak potential of the component Maxwellian that has the lower energy for a bi-Maxwellian function. The amplitude of the curve in the negative direction is normalized to the magnitude of the curve in the positive direction at $E = 0$.

Taking a step further, a two-dimensional (2D) distribution function can be constructed by splicing $-dI/dV$ curves along four different directions. For example, the 2D distribution function in the yz-plane is constructed from the $-dI/dV$ curves in the $\pm y$ and $\pm z$ directions. Figure 6 shows six such polar plots that can be used to visualize the direction of the ion beam propagation. The abscissa and

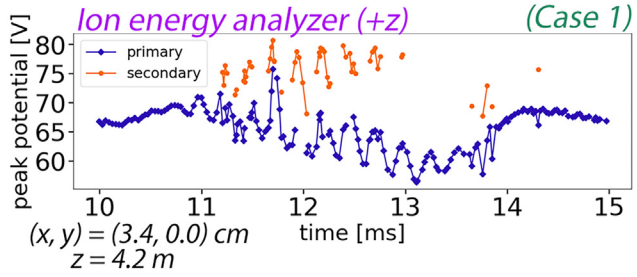

FIG. 4. A plot of the peak potential as a function of time is shown for the background ion distribution (primary) and the beam (secondary). The peak potential of the beam is only plotted when $-dI/dV$ best fits a bi-Maxwellian function.

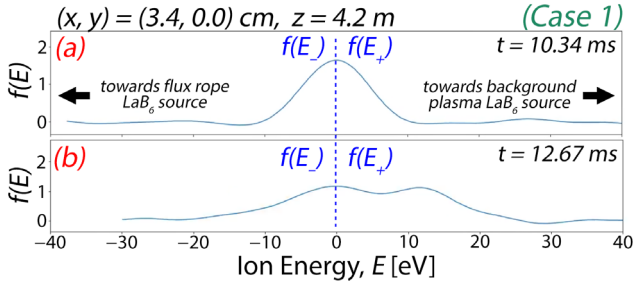

FIG. 5. The IEDFs are constructed by splicing $-dI/dV$ curves measured along the z-direction at two different times. The sign of E represents the direction of the ions, with positive E indicating ions traveling toward the background plasma LaB_6 cathode, and negative indicating the opposite direction. (a) is spliced from two single-peaked distributions, while (b) is spliced from a single-peaked and a bi-Maxwellian function.

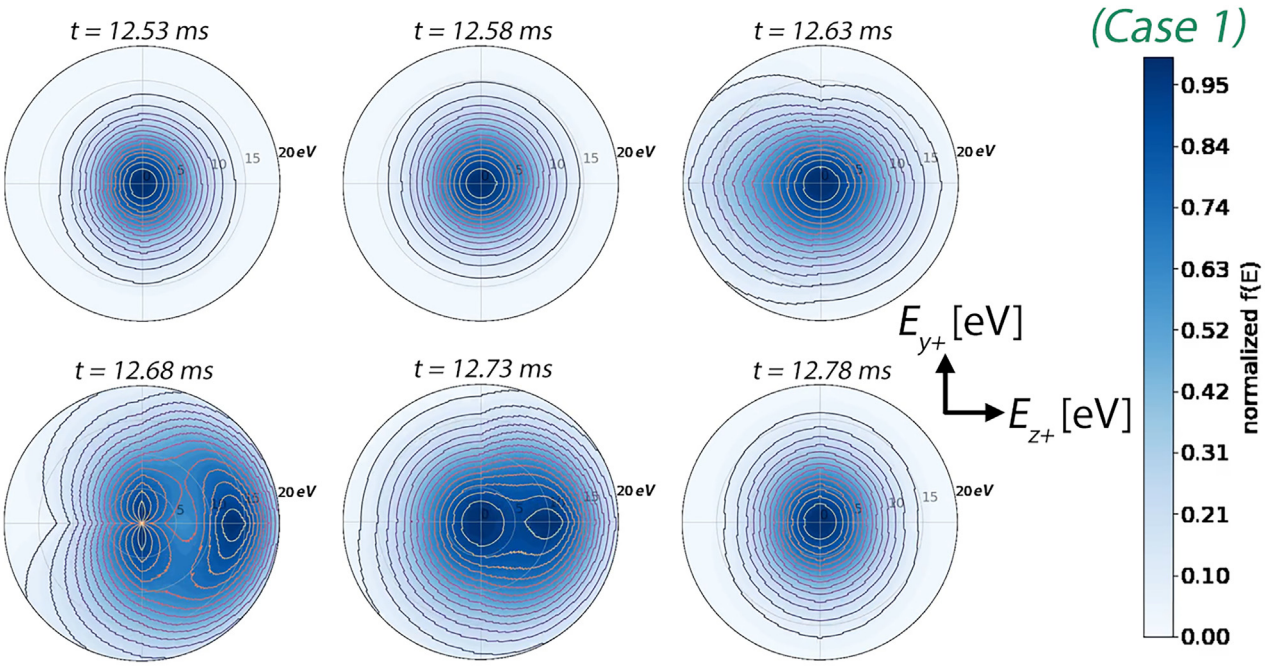

FIG. 6. A time series of polar plots that represent the two-dimensional IEDF constructed from splicing the IEDF along four different directions (i.e., $\pm y$ and $\pm z$). The data in-between angles were interpolated. The time interval corresponds to a single flux rope oscillation ($\Delta t = 0.256$ ms). Each polar plot is normalized to the maxima at the local time. An ion beam in the $+z$ direction can be observed at $t = 12.68$ and 12.73 ms.

ordinate represents data along and across the magnetic field, respectively, while the data in-between the angles are linearly interpolated from the data along the axes. The 15 eV beam shown in Fig. 3 is observed at $t = 12.68$ ms of Fig. 6, which propagates primarily in the $+z$ direction along the background magnetic field. This behavior is also observed from the other ion beams that are periodically produced during the experiment and is reproducible. It suggests that the ion beam is preferentially accelerated along the $+z$ direction and is field-aligned to the background magnetic field.

V. ION TEMPERATURE AND AVERAGE ENERGY

The IEDF is primarily used in the calculation of the average energy $\langle 2E \rangle$, a quantity analogous to the one-dimensional ion temperature kT_i but for a non-Maxwellian IEDF. The presence of a non-Maxwellian IEDF results in an ill-defined ion temperature. The quantity $\langle 2E \rangle$ is derived from the temperature–pressure relationship and the second moment of the velocity distribution function $\langle v^2 \rangle$, i.e.,

$$kT_i = \frac{m\langle v^2 \rangle}{n} \equiv \langle 2E \rangle, \tag{3}$$

where m is the ion mass, and n is the density. By a change of variables to the kinetic energy $E = mv^2/2$ and a splitting of the integral to account for the splicing of two different $-dI/dV$ curves in opposite directions, the average energy is thus expressed as

$$\langle 2E \rangle = \frac{2}{n'}\left(\int_0^\infty dE_+ \sqrt{E_+} f(E_+) + \int_0^\infty dE_- \sqrt{E_-} f(E_-)\right), \tag{4}$$

where $f(E)$ is the IEDF with E is subscripted with $+$ and $-$ to indicate the direction of the ions' velocity, and n' is the normalized density

$$n' = \int_0^\infty dE_+ \frac{1}{\sqrt{E_+}} f(E_+) + \int_0^\infty dE_- \frac{1}{\sqrt{E_-}} f(E_-)\,. \tag{5}$$

The quantity $\langle 2E \rangle$ is then calculated for all time steps when the two flux ropes are present. Figure 7 shows time traces of $\langle 2E \rangle$ for ions moving along the z-direction at two different xy locations, but on the same plane at $z = 4.2$ m. Figure 7(a) is for a location near the center of the two ropes at $(x, y) = (3.4, 0.0)$ cm where reconnection frequently occurs,[25] while Fig. 7(b) is for a point located at the edge of the ropes outside the reconnection region at $(x, y) = (10.0, 0.0)$ cm. The point at the edge of the flux ropes only contains data in the $+z$ direction as opposed to the point in the center which is constructed with data in both the $+z$ and $-z$ directions. In both plots, the data points were conditionally averaged such that the time traces of the two plots are in phase with each other.

The shape and color of each data point depend on whether any of the $-dI/dV$ curves that is used to construct the IEDF best fits a bi-Maxwellian function. The orange, hollow circles indicate data points in which either side of the IEDF fits a bi-Maxwellian function and is likely to contain a beam. The blue, solid diamond-shaped points indicate otherwise where both sides of the IEDF fit single Maxwellians. In addition, the standard error of each data point, which was determined from the fit of the (bi-)Maxwellian function and the error propagation from using Eq. (4), is plotted as the blue shaded region of each plot. Since $\langle 2E \rangle$ converges to the ion temperature kT_i when $f(E)$ is Maxwellian, the blue points that primarily measure the energy of the

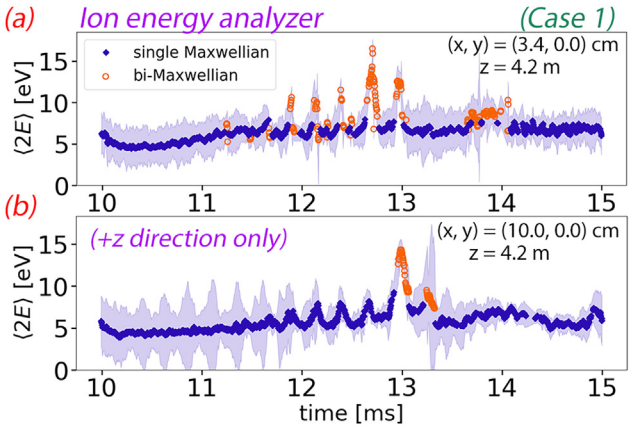

FIG. 7. Plots of the average energy $\langle 2E \rangle$ as a function of time for case 1 at two different locations: (a) near the center of the two ropes where reconnection usually occurs and (b) at a point far from the initial center of the two ropes. The orange data points indicate times at which the IEDF is spliced with a bi-Maxwellian function, while the blue data points indicate times when neither $-dI/dV$ are bi-Maxwellian. The blue shaded region indicates the standard error of the data points. In (b), only data in the $+z$ direction were available for the calculation of $\langle 2E \rangle$.

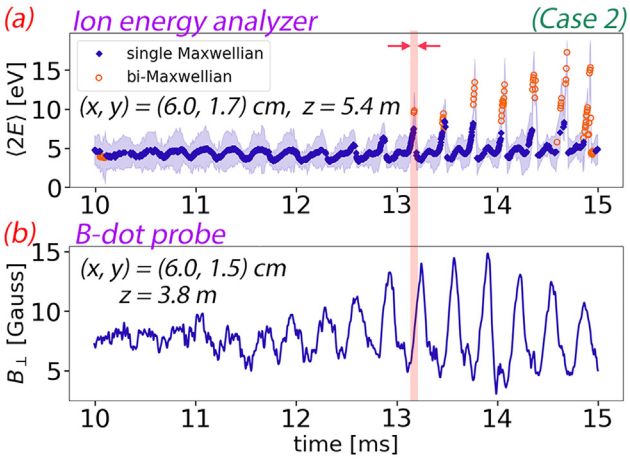

FIG. 8. Plots of (a) the average energy $\langle 2E \rangle$ and (b) the perpendicular magnetic field $B_\perp$ for case 2. The RFEA and B-dot probes were separated $\Delta z = 1.6$ m away from each other. In (a), the blue shaded region indicates the standard error of the data points. The red bar indicates a time interval of interest for Fig. 9.

background distribution of ions can be used to estimate the background ion temperature. In the case of Fig. 7, the background ion temperature is estimated to be between 4 and 8 eV. Above $\langle 2E \rangle = 8$ eV, the data points are mostly orange, in which the overall energy of the ions is increased due to the presence of a beam.

On closer inspection of the orange data points, the increase in the overall energy when the beam appears is primarily due to an acceleration of the ions as opposed to the heating of the beam. Given that the width of a Maxwellian distribution is proportional to its temperature, the widths of both the ion beam and the background ions were consistently found to be comparable to each other within a range of 4–8 V. This can be observed in the $-dI/dV$ plots of Figs. 2(b) and 3.

The $\langle 2E \rangle$ data points between 11.5 and 13.5 ms in Fig. 7 form spiky structures that oscillate at the kink frequency of the ropes ($f = 3.9$ kHz). However, the spiky structures above 8 eV comprised of the orange bi-Maxwellian points occur more frequently at the center [Fig. 7(a)] than at the edge region [Fig. 7(b)] of the two ropes. This suggests that the formation of the ion beam is position-dependent and that is likely to be energized by being in close proximity to the reconnection region. If that is indeed the case, the 14 eV bi-Maxwellian spike formed at the edges of the ropes at 13 ms in Fig. 7(b) may be due to a global rotation of the ropes. In previous studies, it was observed that the ropes rotate with a larger radii as they became more chaotic over time.[30] Thus, in this case, the reconnection region would be allowed to reach the edge region and cause ion beams to form, which are then detected by the RFEA.

VI. THE ION ENERGY DISTRIBUTION FUNCTION IN A RECONNECTING PLASMA

In case 2, the average energy $\langle 2E \rangle$ at a single point near the center of the two ropes $(x, y, z) = (6.0, 1.7, 540)$ cm and the magnetic field in a plane at $z = 3.8$ m were simultaneously measured by the RFEA and a B-dot probe, respectively. The B-dot probe was calibrated by a network analyzer and is sensitive to magnetic fields on the order of 0.1 mG. It is separated $\Delta z = 1.6$ m away from the RFEA and is located closer to the source of the flux ropes. Figure 8 shows a comparison of the time traces of $\langle 2E \rangle$ and the magnitude of the perpendicular magnetic field $B_\perp \left(= \sqrt{B_x^2 + B_y^2} \right)$ when the source of the two ropes is turned on. In Fig. 8(a), the orange data points of $\langle 2E \rangle$ appear between 13 and 15 ms and are highly correlated with the oscillations of $B_\perp$ within the same time interval in Fig. 8(b). Both $\langle 2E \rangle$ and $B_\perp$ oscillate at the kink frequency of the ropes, which in this case is $f = 3.4$ kHz. The large peak-to-peak variation of $B_\perp$ (>10 G) indicates large movements of the ropes and is indirectly correlated with strong reconnection activity.[25] The correlation suggests that an ion beam is produced when the ropes reconnect.

The magnetic field plane at $z = 3.8$ m provides further evidence of reconnection in a plot of the magnetic vector potential A_z as a function of time for the interval indicated by the red bar in Fig. 8 ($t = 13.15$–13.20 ms). The quantity A_z is given by the expression

$$A_z = \frac{\mu_0}{4\pi} \int \frac{J_z(\vec{r}', t')}{|\vec{r} - \vec{r}'|} \, d\vec{r}', \tag{6}$$

where $\vec{r}$ and $\vec{r}'$ are the distances to an observation and source point, respectively, and J_z is the perpendicular current density derived from $\nabla \times \vec{B}$. Figure 9 shows the line contours of A_z at $z = 3.8$ m, which serve as a proxy for the magnetic field lines projected onto the xy-plane due to insufficient data for reconstructing the three-dimensional magnetic field lines of the flux ropes. The reconstruction process requires volumetric datasets consisting of multiple planes of magnetic field data taken along the length of the LAPD, which are not available in this experiment. The xy-coordinates of the RFEA ($z = 5.4$ m) are indicated by the red cross at $t = 13.15$ ms. Two A_z contours that merge and reconnect are highlighted in red to guide the eye.

From previous flux rope experiments, it is known that multiple X-points are located along the length of the two ropes, which serve as potential sites for magnetic reconnection.[31] The presence of

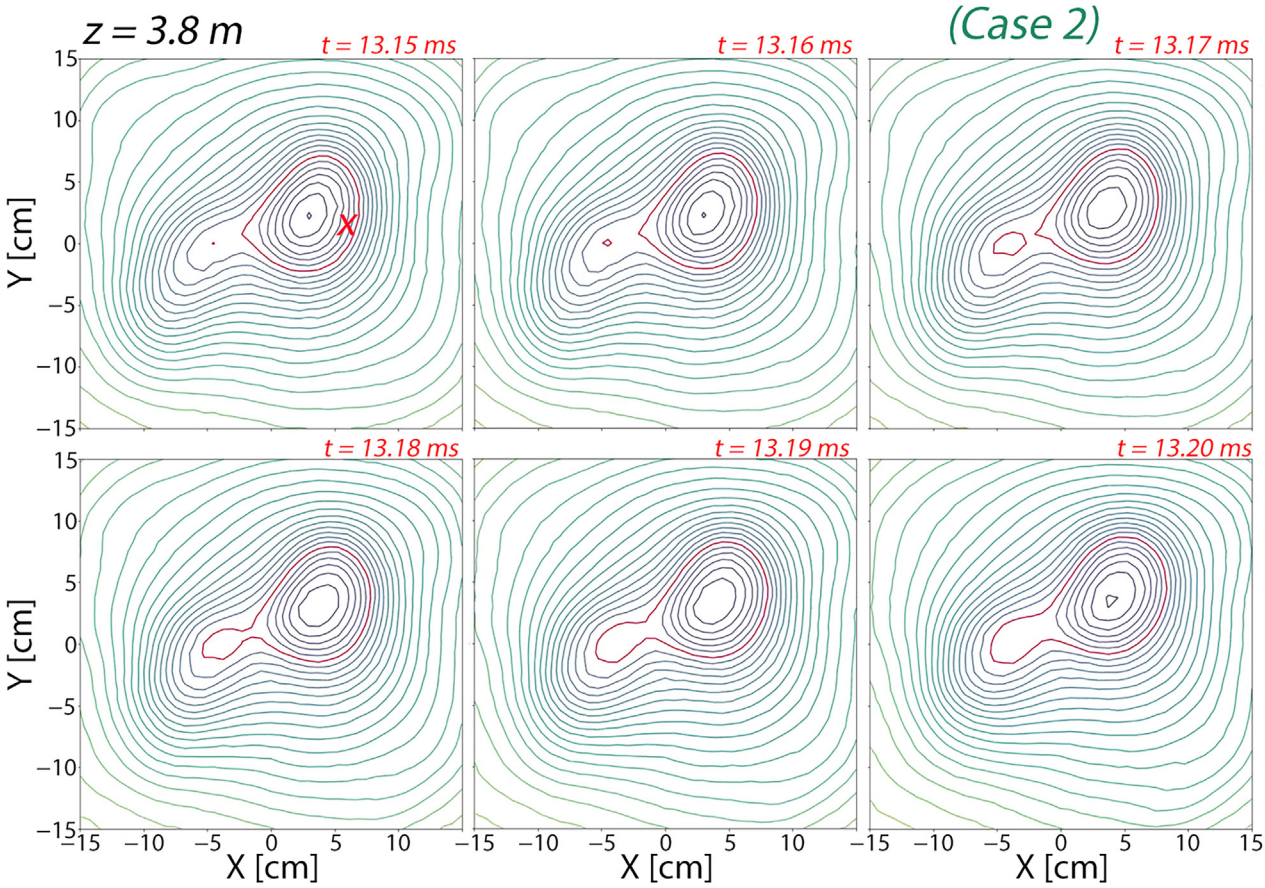

FIG. 9. Contour plots of the vector potential A_z are shown for the time interval indicated by the red bar in Fig. 8. A pair of contour lines that appear to reconnect are colored in red. The position of the RFEA, which simultaneously collected data with the B-dot probe, is marked by the cross at $t = 13.15$ ms.

reconnecting contour lines in Fig. 9 during this time interval thus provides evidence of magnetic reconnection. Furthermore, an inspection of the A_z contour plots at other times reveals periodic merging and reconnecting of field lines, which were also observed at the kink frequency of the ropes ($f = 3.4$ kHz). These periodic reconnection events are correlated with the occurrence of the ion beam.

As an aside, a comparison of the energy released from magnetic reconnection with the energy gain of the ions observed during the appearance of the beam suggests that the acceleration of the ions can be driven by the energy released from magnetic reconnection. These energies can be independently determined from measurements of the magnetic field and the average energy $\langle 2E \rangle$, respectively. For the energy released from magnetic reconnection due to magnetic field annihilation, a current density of $J_z = 12$ A/cm^2, an inductive electric field of $E_z = |dA_z/dt| = 0.18$ V/m, and a reconnection timescale of $\tau_R = 50\,\mu$s, as determined from experimental data, were used. Assuming the energy was dissipated over a reconnection volume of $V_R = 1$ m^3, the energy generated from magnetic field annihilation is $(\tau_R \vec{E} \cdot \vec{J}) V_R = 0.6$ J. This corresponds to the annihilation of $\delta B = 0.23$ G or 0.07% of the total magnetic field ($B_0 = 330$ G), which is consistent in both order and magnitude with previous experimental studies on magnetic reconnection.[32,33] These magnetic fields are significantly smaller than the few hundred Gauss which are annihilated in solar flares,[34] which is estimated to be a third of the total magnetic field.[35]

Next, the typical increase in the average energy of the ions when the beam appears is approximately $\Delta T_i \approx 8$ eV ($6 \rightarrow 14$ eV). Meanwhile, the density of the ions in the beam was estimated by comparing the z-direction IEDF of the beam to that of the primary distribution when $\langle 2E \rangle$ is at a local maximum (e.g., $t = 12.712$ ms). Assuming a beam density of $n_b = 2 \times 10^{11}$ cm^{-3} which is 10% of the plasma density, the effective energy gain of the ions is $(n_b k \Delta T_i) V_R = 0.32$ J. While this density may have been overestimated due to the unknown spread of the beam in the x and y-directions which leads to an overestimate of the energy gain of the ions, it is worth noting that the efficiency of energy transfer from the inductive field to the ions is typically less than 50%.[36,37] This suggests that the energy released from magnetic field annihilation has the potential to create inductive electric fields capable of accelerating ions and forming a beam. However, as will be demonstrated in Sec. VII, the acceleration of the ions cannot be solely attributed to the inductive fields as the space charge fields also play a role in the process.

VII. THREE-DIMENSIONAL GYROKINETIC SIMULATIONS

The data from the RFEA experiment were subsequently compared to three-dimensional gyrokinetic simulations of the two reconnecting flux ropes, which demonstrate that ion acceleration and field-aligned ion beam formation are a consequence of the field-aligned electric potentials that arise from the merging and the magnetic reconnection of the two flux ropes. A gyrokinetic model is well-suited for the large guide field regime of magnetic reconnection where both charged particle species (electrons and ions) are strongly magnetized. In this model, electrons are treated as drift-kinetic particles and ions gyrokinetic, which also include gyro-averaged cross field $\vec{E} \times \vec{B}$ drifts and exact parallel dynamics. The details of the simulation model and basic equations have been given elsewhere.[38,39] The previous model has been extended to include electron–ion collisions, and along with conducting boundary conditions in the x-y plane, logical sheath boundary conditions are employed in the axial z-direction. The axial boundary conditions are such that the flux ropes are line-tied at the $z = 0$ plane and free to move at the furthest axial plane, which is at the mesh anode.

The simulation model allows for the use of realistic parameters when compared to the experiment. The 3D system has spatial scales of dimensions $L_x \times L_y \times L_z = 512\Delta_x \times 512\Delta_y \times 32\Delta_z$, with grid spacings of $\Delta_x = \Delta_y = 0.1\delta_e$ and $\Delta_z = 64.8\delta_e$, where δ_e is the collisionless electron skin depth of approximately 0.53 cm for an electron density of 1×10^{12} cm^{-3}. The simulations were carried out with a maximum of 80 particles per cell. The time step used in the simulation, normalized to the ion cyclotron frequency, i.e., $\omega_{ci}\Delta t_s = 1.0$, corresponds to 0.64 μs, assuming a helium ion mass and a 330 G background magnetic field. The number of time steps varied from $N = 400$, which corresponds to a single rope oscillation of 256 μs, up to 2000 steps. The two flux ropes of diameter $d = 7.6$ cm ($\simeq 20.2\,\delta_e$) and separated by a 3 cm spacing were initialized using approximate fits to the density, temperature, and current profiles taken from the experiment. The initial background plasma temperature ratio was $T_e/T_i = 4$, while the peak flux rope temperature ratio was $T_e/T_i = 1.75$.

The simulations were designed to follow in detail the evolution of a single cycle in the collision and merging of the two oscillating flux ropes. Field and particle data were used to investigate the destruction of magnetic flux in the reconnection region between the two ropes and the subsequent particle distributions affected by the inductive and space charge electric fields. Figure 10 illustrates the merging process of the ropes along the direction of the background magnetic field, showing contours of the vector potential A_z at two different planes but at the same time in the simulation ($t_s = 64\,\mu$s). At $z = 3.8$ m, an X-point is clearly visible in the region between the two ropes, indicating the formation of an induced electric field $-dA_z/dt$.

To illustrate the formation of an energetic ion distribution in the region of the maximum induced electric field in this plane, a group of particles were selected from each of the boxes shown in Fig. 10(a), and their trajectories were followed in time. These boxes correspond to the region in the vicinity of the X-point and away from the two ropes, respectively. The particles were grouped according to their change in velocity, and the ions that experienced an acceleration from the parallel electric field were identified and shown to result in an ion beam. Figure 11 is a plot of the 3D velocity distribution for the ions in these two regions. Ions accelerated by the parallel electric field were colored red, while ions that were not accelerated by the electric field were colored green. In Fig. 11(a), which corresponds to the region near the X-point, the accelerated ions reached maximum speeds of approximately four to five times the ion thermal speed v_{Ti} and were accelerated primarily along the $+z$ direction. A small amount of ion heating was also observed in the accelerated ion distribution. This is roughly consistent with the 15 eV accelerated ion population observed in the experiment where $v/v_{Ti} = 2.7$ (for $T_i = 4$ eV) and is also in the z-direction. In contrast, such ion acceleration was not observed in Fig. 11(b) as there were no enhanced parallel electric fields outside the ropes.

Since the total electric field accelerating the particles consists of both the inductive part ($-dA_z/dt$) and gradient of the local plasma potential ($-\nabla\Phi$), simulations were made with and without these terms present in the particle equations of motion. Their impact on the energetic ion distributions in the region near the X-point is shown in Fig. 12(a), where the inductive field produces an energetic ion population up to approximately 3–4v_{Ti}. In contrast, Fig. 12(b) represents the case with only the space charge contribution to the electric field, which results in a small energy gain of only about v_{Ti}. Their combined effect is originally shown in Fig. 11(a). While the space charge electric field is generally ten times larger than the inductive electric field,[30] the simulations reveal that the inductive electric field has a more dominant effect in the merging region between the two ropes. However, when the initial particle distribution was adjusted such that it encompassed a larger portion of both flux ropes by having a wider box around the merging region, the space charge field enhanced the energy of the beam component by nearly a factor of two when compared to the results of Fig. 12(b). This highlights a critical interplay between both fields in the acceleration of the ions.

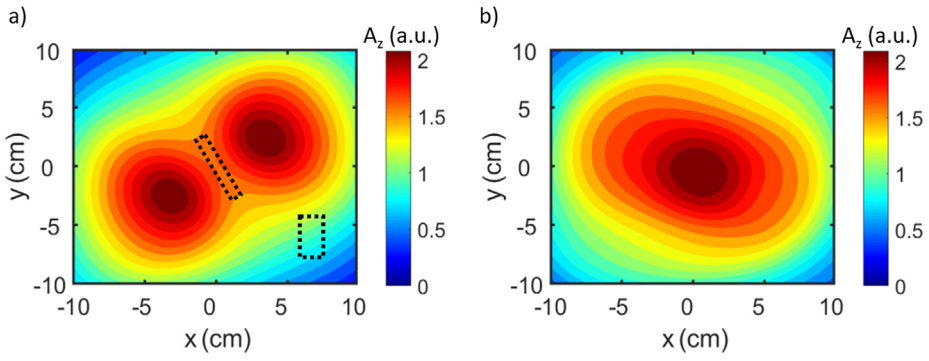

FIG. 10. Contour plots of the vector potential A_z obtained from the 3D gyrokinetic simulation at the same time ($t_s = 64\,\mu$s) but at two different axial planes: (a) $z = 3.8$ m and (b) $z = 8.3$ m from the cathode source. The dotted-line bounding boxes in (a) indicate the regions where particles are initially selected to construct the 3D velocity distributions shown in Fig. 11.

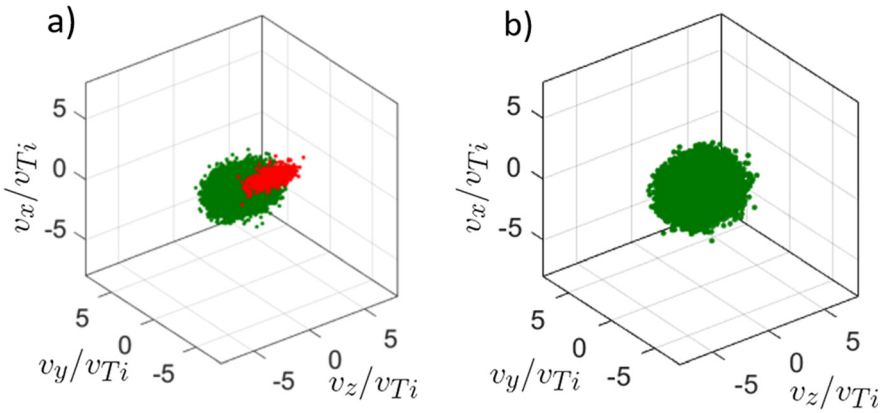

FIG. 11. Plots of the 3D velocity distributions at simulation time $t_s = 96\ \mu$s for particles selected (a) near the X-point, and (b) outside the flux ropes. These two regions are indicated by the dotted-line bounding boxes in Fig. 10(a). The particles that were accelerated by a parallel electric field are colored red, while those that were not are colored green.

The tracks of a few individual ions were subsequently mapped to further understand how the formation of the beam particles, shown in Fig. 11, is influenced by the trajectories of the ions. Starting from the $z = 3.8$ m plane, the motion of four test ions within the vicinity of the X-point was tracked for the duration of the reconnection time ($\Delta t_s = 50\ \mu$s), and the results are plotted in Fig. 13. The path of the ions is shown as black solid lines, while the planes are represented by contour plots of A_z. In this figure, ions located at $z = 3.8$ m begin at the center region between the two ropes where the effect of the inductive field acceleration is dominant. They then drift outward as expected from an outflow of particles from a reconnection region. Interestingly, not all of the ions completely leave the area. Some ions are observed to return to the reconnection region further downstream, including ions that may have lesser energies than than ones observed in beam. We thus hypothesize that the ions that return to the reconnection region are the ones that eventually form the ion beam. These ions are able to accumulate energy from multiple exposures to the inductive field near the X-point and potentially from nearby space charge fields within the ropes.

From these simulation results, the main mechanism for ion acceleration appears to be the total electric field $\vec{E} = -d\vec{A}/dt - \nabla\Phi$. The inductive electric fields $-d\vec{A}/dt$ are produced during magnetic reconnection while the space charge fields $-\nabla\Phi$ presumably by local pressure gradients and charge separation. Ions that are accelerated by the local electric field would gain a potential energy $\Xi = -\int \vec{E} \cdot d\vec{l}$, which is the definition of the reconnection quasipotential.[23] The value of Ξ is obtained by integration along the individual magnetic field lines. Figure 14(a) is a contour plot of Ξ at $z = 3.84$ m, which is approximately at the same z-location as the magnetic field plane from case 2 of the current experiment (see Fig. 9). A positive value of Ξ indicates that ions are accelerated in the $+z$ direction, which is away from the origin of the ropes. Further away from the source of the ropes at $z = 8.32$ m, a contour plot of Ξ is shown in Fig. 14(b). The ropes have rotated, and the accelerating potential fills the central area. This plot is then compared to a plot of the integrated electric field obtained from the 3D gyrokinetic simulation, shown in Fig. 15. The topology and values of the integrated field show remarkable similarity to that of Ξ in Fig. 14(b).

Finally, evidence of reconnection is also provided by the existence of the quasi-separatrix layer (QSL).[22] A QSL greater than 2 indicates rapidly diverging field lines, which can occur when the magnetic field topology suddenly changes. This is a hallmark of reconnection and is shown in Fig. 16. It may be noted that the largest values of Q coincides with the largest values of A_z.

VIII. DISCUSSION

In summary, the data acquired with the RFEA in conjunction with magnetic field measurements show that the energy released from the magnetic reconnection of two colliding flux ropes generate non-Maxwellian IEDFs. During a number of flux rope oscillations that encompasses a reconnection event, an ion beam is drawn out of the

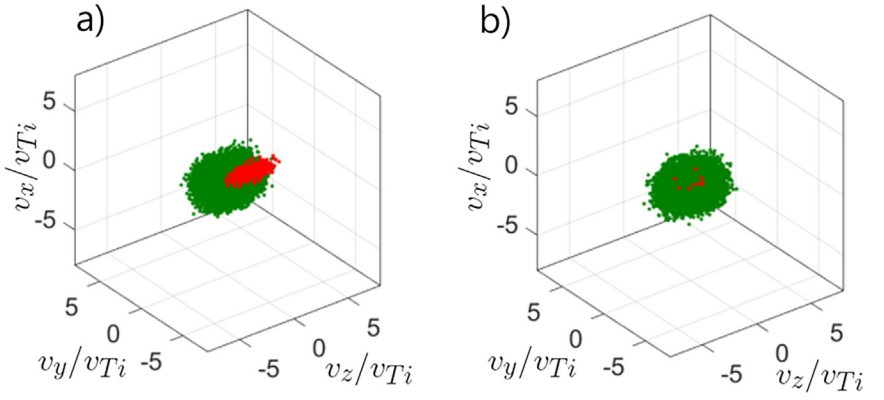

FIG. 12. Plots of the 3D velocity distributions at simulation time $t_s = 96\ \mu$s for particles selected near the X-point to test the effects of simulation with (a) only the inductive electric field $-d\vec{A}/dt$ retained, and (b) only the gradient of electric potential or space charge electric field $-\nabla\Phi$ included. The particles that were accelerated by a parallel electric field are colored red, while those that were not are colored green.

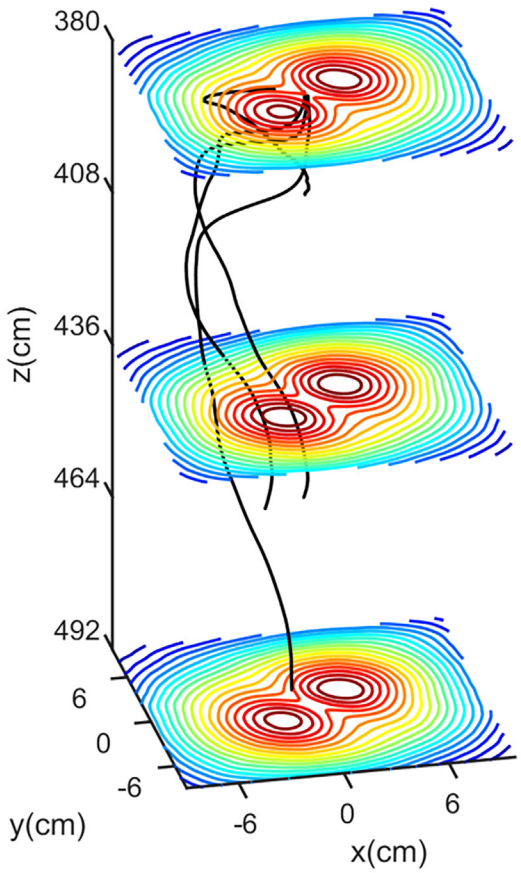

FIG. 13. A 3D plot illustrating the trajectories of four test particles (4, 8, 8, and 12 eV) in the gyrokinetic simulation starting near the X-point at $z = 3.8$ m for a duration of $\Delta t_s = 50\ \mu$s. The particle trajectories are indicated by the black lines, with the longer tracks corresponding to the higher energy test particles, while the cross section of the flux ropes is shown as contour plots of A_z. Most particles tend to drift outward from the reconnection region, but some are able to return to it at a location further downstream.

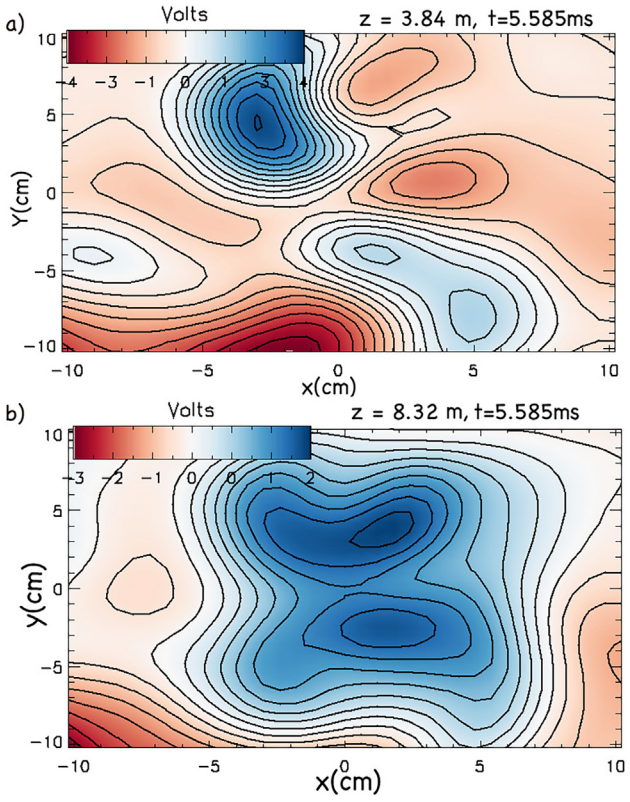

FIG. 14. Experimental contour plots of reconnection quasipotential Ξ, which is calculated from the integral of the total electric field, along the magnetic field lines using data from a previous flux rope experiment[30] in nearly identical experimental conditions. The data are shown at positions (a) $z = 3.84$ m and (b) $z = 8.32$ m.

distribution function. To the authors' knowledge, this is the first observation of a field-aligned ion beam generated in a reconnection experiment. The flux ropes were in a regime where the guide field is strong ($\delta B/B_0 \simeq 4\%$). To date, most spacecraft observations and simulations that deal with Harris-type current sheets have little to no guide fields, such as studies of the Earth's magnetotail using data from the THEMIS spacecraft[40] or studies involving hybrid kinetic-fluid model simulations.[41] In contrast, the studies that do include a strong guide field rarely report ion beam observations.[42–44] For example, Pritchett and Coroniti[45] simulated a current sheet with guide fields of up to five times the transverse field. They observed enhanced parallel electric fields and parallel electron beams, but no ion beams.

In the LAPD two flux rope experiments where the guide fields are considered strong, a significant amount of reconnection activity has been observed.[23,25,31] The reconnection rate R_r is close to the values inferred from 3D simulations[46] and the typical value of 0.1,[47] i.e.,

$$R_r = \frac{\Xi}{LB_0 v_A} \simeq 0.1, \tag{7}$$

where $L = 18$ m is the length of the ropes, B_0 is the reconnecting component of the magnetic field, and v_A is the Alfvén velocity.[23]

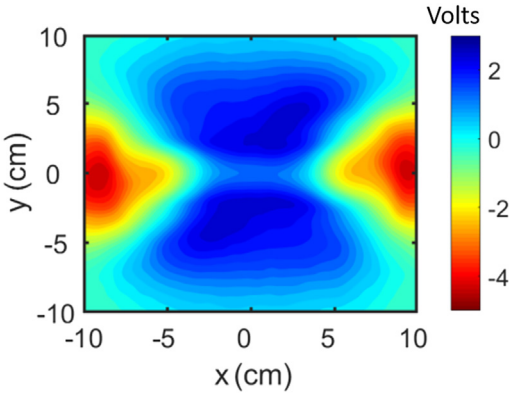

FIG. 15. A contour plot of the integrated electric field obtained from the 3D gyrokinetic simulation at the plane $z = 8.3$ m.

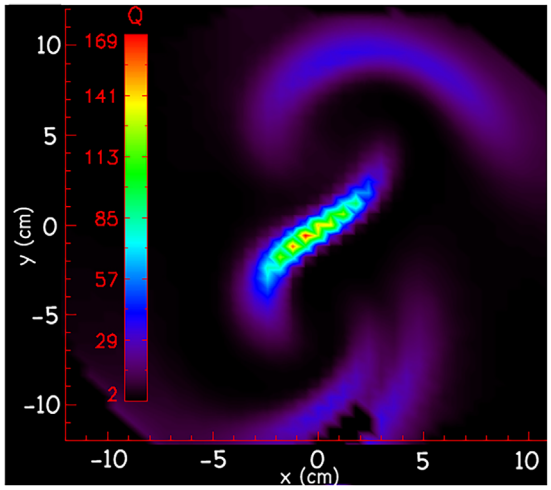

FIG. 16. A contour plot of the QSL at $z = 7$ m evaluated at $t = 5.38$ ms after the start of a previous flux rope experiment.

This is likely due to the enhanced resistivity of the two flux ropes.[30]

In addition, instabilities can also develop structure in the out-of-plane direction,[48] and one possibility is the current-driven ion acoustic instability that propagates longitudinally along the magnetic field.[49] It imparts sufficient momentum to the electrons through ion-acoustic wave–particle interactions in order to violate the electron frozen-in condition[50] and can very effectively and non-resonantly scatter ions across the magnetic field.[51] The ion saturation current associated with the swept Langmuir curves used to determine the electron energy was used to generate frequency spectra, and broadband turbulence from 9.2 kHz to 1.6 MHz was observed only in the spatial region where the flux ropes collided. The upper limit of 1.6 MHz is much lower than the ion plasma frequency $f_{pi} = 148$ MHz. This is not proof that the instability has been directly observed, although it can be generated in a magnetized plasma when there is a relative drift between ions and electrons of order of the sound speed.[52] Such an instability was postulated to create large induced electric fields that resulted in anomalously high AC Kubo resistivity.[30] Waves created by the instability could also be superimposed to form localized potential spikes which could explain the large, negative electric potential structures that appeared previously under similar flux rope conditions.[53]

Overall, the observation of an ion beam that is field-aligned to the background guide field contrasts with previous observations of ions that were locally field-aligned without the presence of a strong guide field,[16,54] or did not appear beam-like despite moving in the out-of-plane direction.[7,9] The ion beams in this experiment are correlated with the collision of the ropes, do not appear to be heated, and have sub-Alfvénic velocities. They are most likely accelerated by the out-of-plane electric fields. An important observation from both experiment and simulation is that both the inductive and space charge electric fields play an important role, and the latter cannot be ignored. The formation of the beam is a non-local process involving both inductive and space charge electric fields which are dominant at different locations. Incidentally, previous experiments discovered that the fluid form of Ohm's law is non-local and cannot be used to calculate the resistivity.[30] These observations provide a basis for the study of ion dynamics in systems that are inherently described by three-dimensional models of reconnection.

ACKNOWLEDGMENTS

The authors would like to thank Patrick Pribyl for his expertise in electronics as well as Zoltan Lucky, Marvin Drandell, and Tai Ly for their technical support and assistance. The authors would also like to thank the first referee for their comments on the ion acceleration. The work was performed at the Basic Plasma Science Facility at UCLA, which is funded by the United States Department of Energy and the National Science Foundation.

AUTHOR DECLARATIONS

Conflict of Interest

The authors have no conflicts to disclose.

Author Contributions

Shawn Wenjie Tang: Conceptualization (equal); Data curation (equal); Formal analysis (equal); Investigation (equal); Methodology (equal); Software (equal); Validation (equal); Visualization (equal); Writing – original draft (lead); Writing – review & editing (equal). **Walter Gekelman:** Conceptualization (equal); Data curation (equal); Formal analysis (equal); Investigation (equal); Methodology (equal); Software (equal); Supervision (equal); Validation (equal); Visualization (equal); Writing – original draft (supporting); Writing – review & editing (equal). **Richard D. Sydora:** Formal analysis (equal); Software (equal); Visualization (equal); Writing – review & editing (equal).

DATA AVAILABILITY

The data that support the findings of this study are available from the corresponding author upon reasonable request.

REFERENCES

[1]V. M. Vasyliunas, "Theoretical models of magnetic field line merging," Rev. Geophys. **13**, 303–336, https://doi.org/10.1029/RG013i001p00303 (1975).
[2]J. F. Drake and M. Swisdak, "Ion heating and acceleration during magnetic reconnection relevant to the corona," Space Sci. Rev. **172**, 227–240 (2012).
[3]J. T. Dahlin, J. F. Drake, and M. Swisdak, "The mechanisms of electron heating and acceleration during magnetic reconnection," Phys. Plasmas **21**, 092304 (2014).
[4]A. Vaivads, Y. Khotyaintsev, M. André, and R. A. Treumann, "Plasma waves near reconnection sites," in *Geospace Electromagnetic Waves and Radiation* (Springer, 2006), pp. 251–269.
[5]M. Fujimoto, I. Shinohara, and H. Kojima, "Reconnection and waves: A review with a perspective," Space Sci. Rev. **160**, 123–143 (2011).
[6]Y. Ono, M. Yamada, T. Akao, T. Tajima, and R. Matsumoto, "Ion acceleration and direct ion heating in three-component magnetic reconnection," Phys. Rev. Lett. **76**, 3328 (1996).
[7]S. C. Hsu, T. A. Carter, G. Fiksel, H. Ji, R. M. Kulsrud, and M. Yamada, "Experimental study of ion heating and acceleration during magnetic reconnection," Phys. Plasmas **8**, 1916–1928 (2001).
[8]M. R. Brown, "Experimental studies of magnetic reconnection," Phys. Plasmas **6**, 1717–1724 (1999).
[9]M. R. Brown, C. D. Cothran, M. Landreman, D. Schlossberg, W. H. Matthaeus, G. Qin, V. S. Lukin, and T. Gray, "Energetic particles from three-dimensional magnetic reconnection events in the Swarthmore Spheromak Experiment," Phys. Plasmas **9**, 2077–2084 (2002).

[10]D. I. Pontin, "Three-dimensional magnetic reconnection regimes: A review," Adv. Space Res. **47**, 1508–1522 (2011).
[11]D. H. Mackay and A. A. van Ballegooijen, "Models of the large-scale corona. I. Formation, evolution, and liftoff of magnetic flux ropes," Astrophys. J. **641**, 577–589 (2006).
[12]M. Janvier, "Three-dimensional magnetic reconnection and its application to solar flares," J. Plasma Phys. **83**, 535830101 (2017).
[13]D. D. Ryutov, I. Furno, T. P. Intrator, S. Abbate, and T. Madziwa-Nussinov, "Phenomenological theory of the kink instability in a slender plasma column," Phys. Plasmas **13**, 032105 (2006).
[14]B. W. Lites, "Magnetic flux ropes in the solar photosphere: The vector magnetic field under active region filaments," Astrophys. J. **622**, 1275–1291 (2005).
[15]T. Li, E. Priest, and R. Guo, "Three-dimensional magnetic reconnection in astrophysical plasmas," Proc. R. Soc. A **477**, 20200949 (2021).
[16]M. Hoshino, T. Mukai, T. Yamamoto, and S. Kokubun, "Ion dynamics in magnetic reconnection: Comparison between numerical simulation and Geotail observations," J. Geophys. Res. Space Phys. **103**, 4509–4530, https://doi.org/10.1029/97JA01785 (1998).
[17]T. Nagai, I. Shinohara, and S. Zenitani, "Ion acceleration processes in magnetic reconnection: Geotail observations in the magnetotail," J. Geophys. Res. Space Phys. **120**, 1766–1783, https://doi.org/10.1002/2014JA020737 (2015).
[18]W. Gekelman, P. Pribyl, Z. Lucky, M. Drandell, D. Leneman, J. Maggs, S. Vincena, B. van Compernolle, S. K. P. Tripathi, G. Morales *et al.*, "The upgraded large plasma device, a machine for studying frontier basic plasma physics," Rev. Sci. Instrum. **87**, 025105 (2016).
[19]A. R. Yeates and G. Hornig, "Unique topological characterization of braided magnetic fields," Phys. Plasmas **20**, 012102 (2013).
[20]C. Prior and A. R. Yeates, "Quantifying reconnective activity in braided vector fields," Phys. Rev. E **98**, 013204 (2018).
[21]V. S. Titov, T. G. Forbes, E. R. Priest, Z. Mikić, and J. A. Linker, "Slip-squashing factors as a measure of three-dimensional magnetic reconnection," Astrophys. J. **693**, 1029–1044 (2009).
[22]E. E. Lawrence and W. Gekelman, "Identification of a quasiseparatrix layer in a reconnecting laboratory magnetoplasma," Phys. Rev. Lett. **103**, 105002 (2009).
[23]W. Gekelman, T. De Haas, W. Daughton, B. Van Compernolle, T. Intrator, and S. Vincena, "Pulsating magnetic reconnection driven by three-dimensional flux-rope interactions," Phys. Rev. Lett. **116**, 235101 (2016).
[24]B. Van Compernolle and W. Gekelman, "Morphology and dynamics of three interacting kink-unstable flux ropes in a laboratory magnetoplasma," Phys. Plasmas **19**, 102102 (2012).
[25]W. Gekelman, T. DeHaas, C. Prior, and A. Yeates, "Using topology to locate the position where fully three-dimensional reconnection occurs," SN Appl. Sci. **2**, 1–15 (2020).
[26]S. W. Tang and W. Gekelman, "A retarding field energy analyzer for measuring the ion energy distribution function of a two flux rope experiment on the Large Plasma Device," (unpublished).
[27]E. T. Everson, P. Pribyl, C. G. Constantin, A. Zylstra, D. Schaeffer, N. L. Kugland, and C. Niemann, "Design, construction, and calibration of a three-axis, high-frequency magnetic probe (B-dot probe) as a diagnostic for exploding plasmas," Rev. Sci. Instrum. **80**, 113505 (2009).
[28]T. DeHaas, W. Gekelman, and B. Van Compernolle, "Experimental study of a linear/non-linear flux rope," Phys. Plasmas **22**, 082118 (2015).
[29]C. A. Robertson and J. G. Fryer, "Some descriptive properties of normal mixtures," Scand. Actuar. J. **1969**, 137–146.
[30]W. Gekelman, T. DeHaas, P. Pribyl, S. Vincena, B. Van Compernolle, R. Sydora, and S. K. P. Tripathi, "Nonlocal Ohms law, plasma resistivity, and reconnection during collisions of magnetic flux ropes," Astrophys. J. **853**, 33 (2018).
[31]W. Gekelman, E. Lawrence, A. Collette, S. Vincena, B. Van Compernolle, P. Pribyl, M. Berger, and J. Campbell, "Magnetic field line reconnection in the current systems of flux ropes and Alfvén waves," Phys. Scr. **2010**, 014032.
[32]T. DeHaas and W. Gekelman, "Helicity transformation under the collision and merging of two magnetic flux ropes," Phys. Plasmas **24**, 072108 (2017).
[33]R. L. Stenzel, W. Gekelman, and N. Wild, "Magnetic field line reconnection experiments, 4. Resistivity, heating, and energy flow," J. Geophys. Res. Space Phys. **87**, 111–117, https://doi.org/10.1029/JA087iA01p00111 (1982).
[34]E. N. Parker, "Acceleration of cosmic rays in solar flares," Phys. Rev. **107**, 830 (1957).
[35]A. G. Emslie, "An interacting loop model of solar flare bursts," Astrophys. Lett. **22**, 171–177 (1981).
[36]M. Yamada, J. Yoo, J. Jara-Almonte, H. Ji, R. M. Kulsrud, and C. E. Myers, "Conversion of magnetic energy in the magnetic reconnection layer of a laboratory plasma," Nat. Commun. **5**, 4774 (2014).
[37]M. J. Aschwanden, A. Caspi, C. M. S. Cohen, G. Holman, J. Jing, M. Kretzschmar, E. P. Kontar, J. M. McTiernan, R. A. Mewaldt, A. O'Flannagain *et al.*, "Global energetics of solar flares. V. Energy closure in flares and coronal mass ejections," Astrophys. J. **836**, 17 (2017).
[38]R. D. Sydora, "Nonlinear dynamics of small-scale magnetic islands in high temperature plasmas," Phys. Plasmas **8**, 1929–1934 (2001).
[39]R. D. Sydora, G. J. Morales, J. E. Maggs, and B. V. Compernolle, "Three-dimensional gyrokinetic simulation of the relaxation of a magnetized temperature filament," Phys. Plasmas **22**, 102303 (2015).
[40]J. P. Eastwood, M. V. Goldman, H. Hietala, D. L. Newman, R. Mistry, and G. Lapenta, "Ion reflection and acceleration near magnetotail dipolarization fronts associated with magnetic reconnection," J. Geophys. Res. Space Phys. **120**, 511–525, https://doi.org/10.1002/2014JA020516 (2015).
[41]R.-F. Lottermoser, M. Scholer, and A. P. Matthews, "Ion kinetic effects in magnetic reconnection: Hybrid simulations," J. Geophys. Res. Space Phys. **103**, 4547–4559, https://doi.org/10.1029/97JA01872 (1998).
[42]P. Ricci, J. U. Brackbill, W. Daughton, and G. Lapenta, "Collisionless magnetic reconnection in the presence of a guide field," Phys. Plasmas **11**, 4102–4114 (2004).
[43]J. D. Huba, "Hall magnetic reconnection: Guide field dependence," Phys. Plasmas **12**, 012322 (2005).
[44]G. Lapenta, S. Markidis, A. Divin, M. Goldman, and D. Newman, "Scales of guide field reconnection at the hydrogen mass ratio," Phys. Plasmas **17**, 082106 (2010).
[45]P. L. Pritchett and F. V. Coroniti, "Three-dimensional collisionless magnetic reconnection in the presence of a guide field," J. Geophys. Res. Space Phys. **109**, 120033239, https://dx.doi.org/10.1029/2003JA009999 (2004).
[46]Y.-H. Liu, W. Daughton, H. Karimabadi, H. Li, and V. Roytershteyn, "Bifurcated structure of the electron diffusion region in three-dimensional magnetic reconnection," Phys. Rev. Lett. **110**, 265004 (2013).
[47]P. A. Cassak, Y.-H. Liu, and M. A. Shay, "A review of the 0.1 reconnection rate problem," J. Plasma Phys. **83**, 715830501 (2017).
[48]A. Zeiler, D. Biskamp, J. F. Drake, B. N. Rogers, M. A. Shay, and M. Scholer, "Three-dimensional particle simulations of collisionless magnetic reconnection," J. Geophys. Res. Space Phys. **107**, SMP–6, https://doi.org/10.1029/2001JA000287 (2002).
[49]F. V. Coroniti and A. Eviatar, "Magnetic field reconnection in a collisionless plasma," Astrophys. J. Suppl. Ser. **33**, 189–210 (1977).
[50]P. Petkaki and M. P. Freeman, "Nonlinear dependence of anomalous ion-acoustic resistivity on electron drift velocity," Astrophys. J. **686**, 686 (2008).
[51]R. L. Stenzel and W. Gekelman, "Diffusion and scattering of test particles in a turbulent plasma," Phys. Rev. Lett. **40**, 550 (1978).
[52]W. Gekelman and R. L. Stenzel, "Ion sound turbulence in a magnetoplasma," Phys. Fluids **21**, 2014–2023 (1978).
[53]W. Gekelman, S. W. Tang, T. DeHaas, S. Vincena, P. Pribyl, and R. Sydora, "Spiky electric and magnetic field structures in flux rope experiments," Proc. Natl. Acad. Sci. U. S. A. **116**, 18239–18244 (2018).
[54]B. Lavraud, R. Kieokaew, N. Fargette, P. Louarn, A. Fedorov, N. André, G. Fruit, V. Génot, V. Réville, A. P. Rouillard, I. Plotnikov, E. Penou, A. Barthe, L. Prech, C. J. Owen, R. Bruno, F. Allegrini, M. Berthomier, D. Kataria, S. Livi, J. M. Raines, R. D'Amicis, J. P. Eastwood, C. Froment, R. Laker, M. Maksimovic, F. Marcucci, S. Perri, D. Perrone, T. D. Phan, D. Stansby, J. Stawarz, S. Toledo-Redondo, A. Vaivads, D. Verscharen, I. Zouganelis, V. Angelini, V. Evans, T. S. Horbury, and H. O'Brien, "Magnetic reconnection as a mechanism to produce multiple thermal proton populations and beams locally in the solar wind," Astron. Astrophys. **656**, A37 (2021).